Bimodal pattern of seismicity detected at the ocean margin of an Antarctic ice shelf

Denis Lombardi, Lionel Benoit, Thierry Camelbeeck, Olivier Martin, Christophe Meynard, Christian Thom

HAL Id: insu-03581312

https://insu.hal.science/insu-03581312

Submitted on 19 Feb 2022

Bimodal pattern of seismicity detected at the ocean margin of an Antarctic ice shelf

Denis Lombardi,[1,2] Lionel Benoit,[3,*] Thierry Camelbeeck,[1] Olivier Martin,[3] Christophe Meynard[3] and Christian Thom[3]

[1]*Royal Observatory of Belgium, 03 av. circulaire, 1180 Brussels, Belgium. E-mail: lombardi@ipgp.fr*
[2]*Institut de Physique du Globe de Paris, 01 rue Jussieu, F-75005 Paris, France*
[3]*Université Paris-Est / IGN / LOEMI, 73 av. de Paris, F-94160 St-Mandé, France*

SUMMARY

In Antarctica, locally grounded ice, such as ice rises bordering floating ice shelves, plays a major role in the ice mass balance as it stabilizes the ice sheet flow from the hinterland. When in direct contact with the ocean, the ice rise buttressing effect may be altered in response of changing ocean forcing. To investigate this vulnerable zone, four sites near the boundary of an ice shelf with an ice rise promontory in Dronning Maud Land, East-Antarctica were monitored for a month in early 2014 with new instruments that include both seismic and GPS sensors. Our study indicated that this transition zone experiences periodic seismic activity resulting from surface crevassing during oceanic tide-induced flexure of the ice shelf. The most significant finding is the observation of apparent fortnightly tide-modulated low-frequency, long-duration seismic events at the seaward front of the ice rise promontory. A basal origin of these events is postulated with the ocean water surge at each new spring tide triggering basal crevassing or basal slip on a local bedrock asperity. Detection and monitoring of such seismicity may help identifying ice rise zones vulnerable to intensified ocean forcing.

Key words: Seismic cycle; Transient deformation; Tides and planetary waves; Glaciology; Fracture and flow; Antarctica.

1 INTRODUCTION

In East Antarctica, the coastal region of Dronning Maud Land (DML) is characterized by the presence of small ice shelves ($<40\,000$ km^2) intercalated by numerous ice rises, small-scale features where ice is locally grounded on elevated bedrock topography (Fig. 1). Exerting strong ice flow compression and friction on their upstream saddle and on their margin respectively, ice rises provide a significant buttress to the ice sheet flow. For a comprehensive description of ice rises see the recent review of Matsuoka *et al.* (2015). Recent studies suggest that the glacial system of DML is close to the ice mass balance equilibrium and focus on the importance of the presence of numerous ice rises to stabilize the DML coastal ice shelves (Kim *et al.* 2001; Drews *et al.* 2013; Callens *et al.* 2015; Drews *et al.* 2015). Fed primarily by the 500 km long Sør Rondane ice stream (or sometimes referred to as West Raghnild Glacier) the Roi Baudouin ice shelf has been recognized as a major drainage ice stream of the DML region (Rignot *et al.* 2011). It is receiving more scientific attention since the establishment in 2009

of the near-by (150 km) Princess Elisabeth Belgian research station (Matsuoka *et al.* 2012; Pattyn *et al.* 2012; Drews *et al.* 2015). To gain further insight in the interactions of this ice shelf with the austral ocean and in the role of ice rises, we conducted in early 2014 an experiment recording simultaneous local ice flow and seismicity at a bordering unnamed ice rise promontory (hereafter referred as 'IRP'). The study presented here provides concurrently the validation of a newly designed GPS-seismic data logger and the feasibility of its installation in harsh environment.

2 EXPERIMENT AND DATA SET

From mid-January to mid-February 2014, four sites (hereafter referred to as site#) were equipped with a 1 s short-period seismic sensor (Lennartz LE3Dlite) which benefits from a flat spectral amplitude response between 1 and 80 Hz. Each of the seismic sensors was collocated with a single-frequency GPS module (u-blox LEA-6T) embedded into a device named GEOCUBE and developed by the French National Institute of Geography and Forest Information (Benoit *et al.* 2015a,b). The strong advantages of the GEOCUBE over commercial data loggers reside in its light weight, low-cost and low-energy consumption making it suitable for rapid deployment in cold, harsh and hazardous terrain. Being the first polar experiment

* Université de Lausanne, IDYST, Quartier Mouline, 1015 Lausanne, Switzerland.
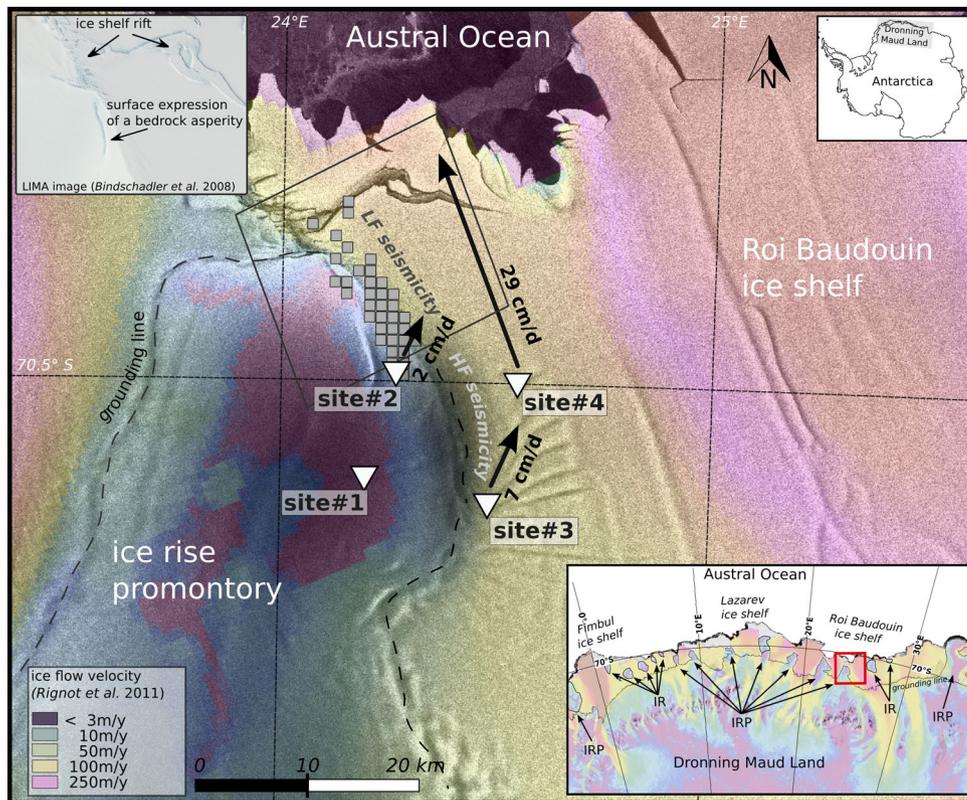
Figure 1. Location map of the study area: an unnamed ice rise promontory of eastern Dronning Maud Land (DML), East Antarctica. The four sites are marked with white triangles and named "site#". For each site, except the reference site#1, the length of each arrow shows the observed mean ice flow velocity while the orientation of the arrow shows the observed mean ice flow direction observed during the experiment. Background colours represent the ice flow speed estimated from satellite observations (Rignot *et al.* 2011). The black shaded zone between site#2 and site#3 denotes the area affected by HF seismicity. Confidence region for the location of LF seismicity (north of site#2) is marked by grey squares. The top-left inset shows the LIMA visible image (Bindschadler *et al.* 2008) for the area marked by a large rectangle north of site#2. The lower-right inset shows the distribution of the numerous ice rises (IRs) and ice rise promontories (IRPs) in the DML, East Antarctica. The red rectangle indicates the study area. The top-right inset shows the location of the DML on the Antarctica continent.

using the GEOCUBE, this study provides a substantial assessment of its robustness to extreme weather conditions. One instrument was installed at the crest of the IRP (site#1), *ca.* 10 km west of the grounding line. Two instruments were at the grounding line transition zone (site#2 and site#3), 1–2 km away from it, on each side. One last instrument was on the freely floating ice (site#4), about 7 km east of the grounding line. The four instruments functioned properly for a minimum of 13 d (site#1) and a maximum of 24 d (site#3 and site#4), the difference in the duration being due to varying battery capacity and voltage discharge rate (no solar panels were used). The relative positioning is performed using the GEOCUBE of site#1 as a reference location, assuming its location on the IRP is non-moving over the 13 d, an assumption validated by satellite observations (Rignot *et al.* 2011, background colours of Fig. 1). The large distances (or baselines) between GEOCUBEs (>5 km), resulting in large effects of ionospheric perturbations on our single-frequency GPS data set, hamper fixing the ambiguities inherent to carrier-phase measurements. Consequently, we cannot use standard differential GPS positioning. To overcome this limitation, data were processed using ambiguity-free phase triple difference (Remondi & Brown 2000). Detrended position time-series of the GEOCUBE from site#2 were used to estimate the precision on the position which equals 3.5 and 4 cm for the horizontal and vertical components, respectively. In a first step, the seismic data set was bandpass filtered between 1 and 10 Hz in order to minimize the strong signal from microseismic noise (below 1 Hz) and signal from local perturbations such as thermal ice microcracks or wind-induced effects on

the equipment (above 10 Hz). Note that, regardless of the source of seismic noise, extraction of low-frequency (LF) content data below 1 Hz is hampered by the short-period characteristics of the seismic sensor used here. To identify local seismic events we computed the ratio of a short-term window average over a long-term window average (STA/LTA; Allen 1978). We used here window lengths of 1 s and 40 s for the STA and LTA, respectively. Subsequently, seismic signals with longest duration (>15 s) were used as templates in a matched filter in order to detect repeating seismic events. In this search, only signal templates recorded at site#2 and site#4 generated successful matches, possibly due to their signal-to-noise ratios higher than for the other two sites. All seismic signals with correlation coefficient $r > 0.4$ for at least one station were kept at first and were then visually inspected in their bandpass filtered and original raw forms. Rejection of a few spurious signals or signals from teleseismic events was required to build a reliable data set of local seismic events. From this procedure, two major types of local seismic events were identified and are described in the following section.

3 RESULTS

3.1 GPS observations

From the three moving sites (Fig. 1), site#2, located about 2 km inland from the groundling line, presents negligible motion
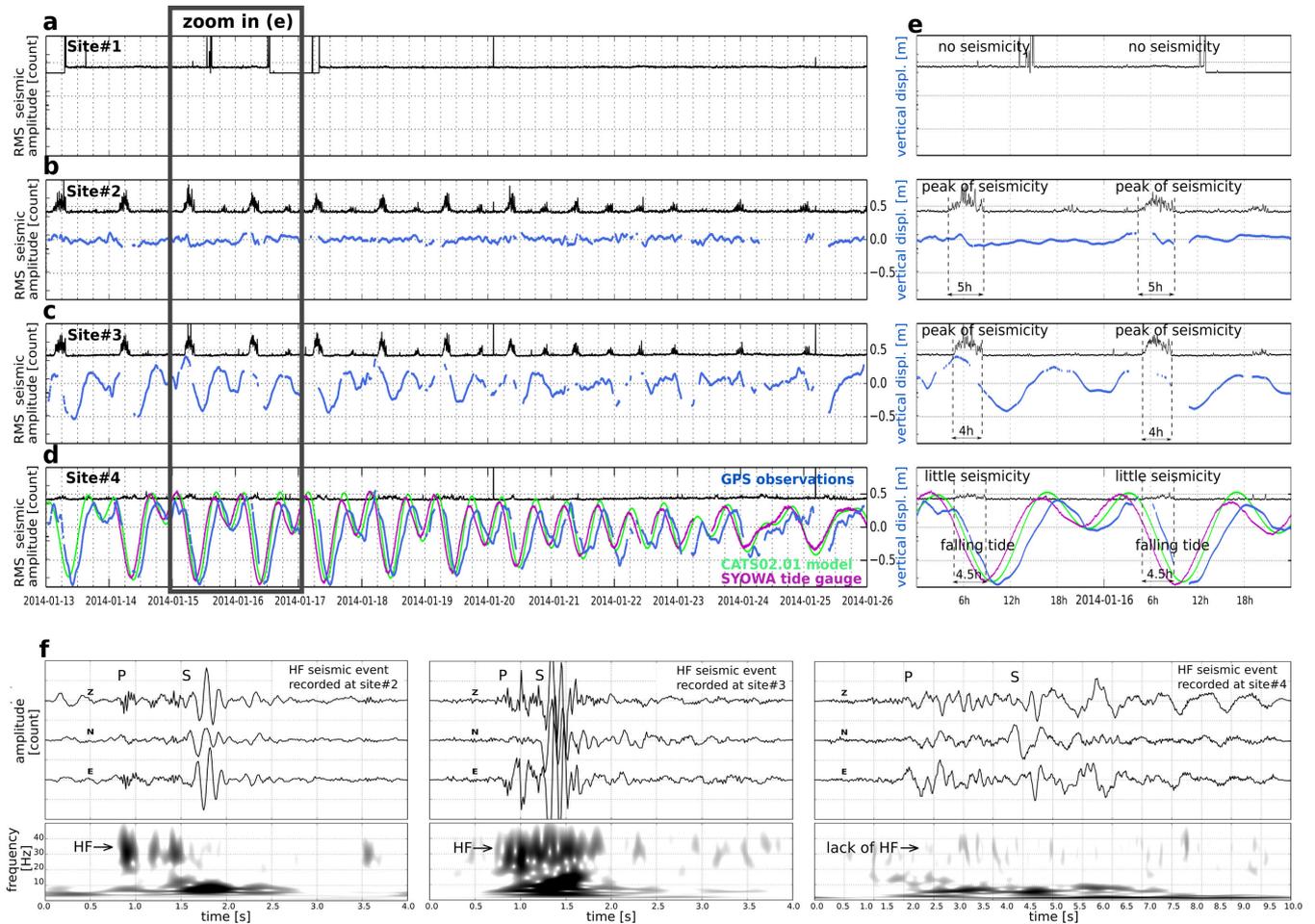
Figure 2. RMS seismic amplitude (black line) and vertical displacement (blue) recorded at the four sites (a–d). Site#1 is used as reference site for differential displacement calculation and therefore does not present any displacement measurements (a). CATS02.01 model tide heights (green) and the tide gauge measurements (purple) at SYOWA Japanese station (located 650 km eastwards) are shown on the top of the site#4 vertical displacements (d). An example of a 2 d long record clearly shows the increased seismicity during the first 4–5 hr of each falling tide (e). When present on 1 trace only (e.g. in panel a) spikes are related to sensor malfunctioning while when present on all sensors they indicate seismic signal from teleseismic events. Examples of three component (Z, N, E) seismic traces for three different HF events for sites #2, #3 and #4 and their associated spectrograms are shown in panel (f). Note that while seismic amplitude scale is the same for the three sites, the timescale is different for site#4.

(1.9 cm d^{-1}) directed towards the ice shelf (N24°). The observed stable vertical positions indicate site#2 does not experience the tide influence attesting this site is definitely grounded and that tidal forcing does not propagate here far inland on the IRP (Fig. 2b). Located about 1 km on the ice shelf side of the grounding line, site#3 experiences 7 cm d^{-1} of motion directed towards N18° (Fig. 1) similarly to site#2. By contrast, it exhibits large vertical displacement (80 cm maximum peak-to-peak, Fig. 2c) contrasting with its relatively small horizontal motion. These observations suggest site#3 is lying on the floating ice, however, its horizontal ice flow presumably results from a combination of two conflicting ice motion: the IRP downslope radial ice flow (directed here roughly towards ESE) and the ice shelf flow (i.e. towards NNW, as estimated by satellite observations). Site#4 located 7 km east of the grounding line exhibits a rapid horizontal motion of 29 cm d^{-1} directed along the main ice flow (N334°). Assuming constant velocity over the year, such a value would lead to a 106 m yr^{-1} ice flow velocity, in agreement with satellite observations (Rignot *et al*. 2011). Site#4 presents fairly large and periodic vertical displacement (140 cm maximum peak-to-peak) which matches fairly well (correlation co-

efficient $r = 0.79$, amplitude misfit $= 10$ cm when the time-series are aligned in phase) with the modelled local sea level variations hereafter referred to as CATS02.01 model (Padman *et al*. 2002, Fig. 2d). Such a remarkable match reflects the weak dissipation of tidal energy through the subshelf water cavity at least within the first 30 km from the ice shelf front. Our tidally induced GPS-measured vertical displacements lag the CATS02.01 model by about 1 hr. The favoured cause for such a large time lag is that the CATS02.01 model may lack assimilated local subice shelf bathymetry information in this particular region together with the non-consideration of nonlinear interactions between ice shelf and tide at the ice shelf shear margins (Padman *et al*. 2002). Assimilating such GPS data from a rarely visited ice shelf would improve the spatial coverage of the CATS02.01 tide model.

3.2 HF seismicity

Seismic event detection evidences two main types of local activity. The first kind consists of individual high-frequency (HF; up to Nyquist frequency i.e. 50 Hz) short-duration events (2–3 s) with the
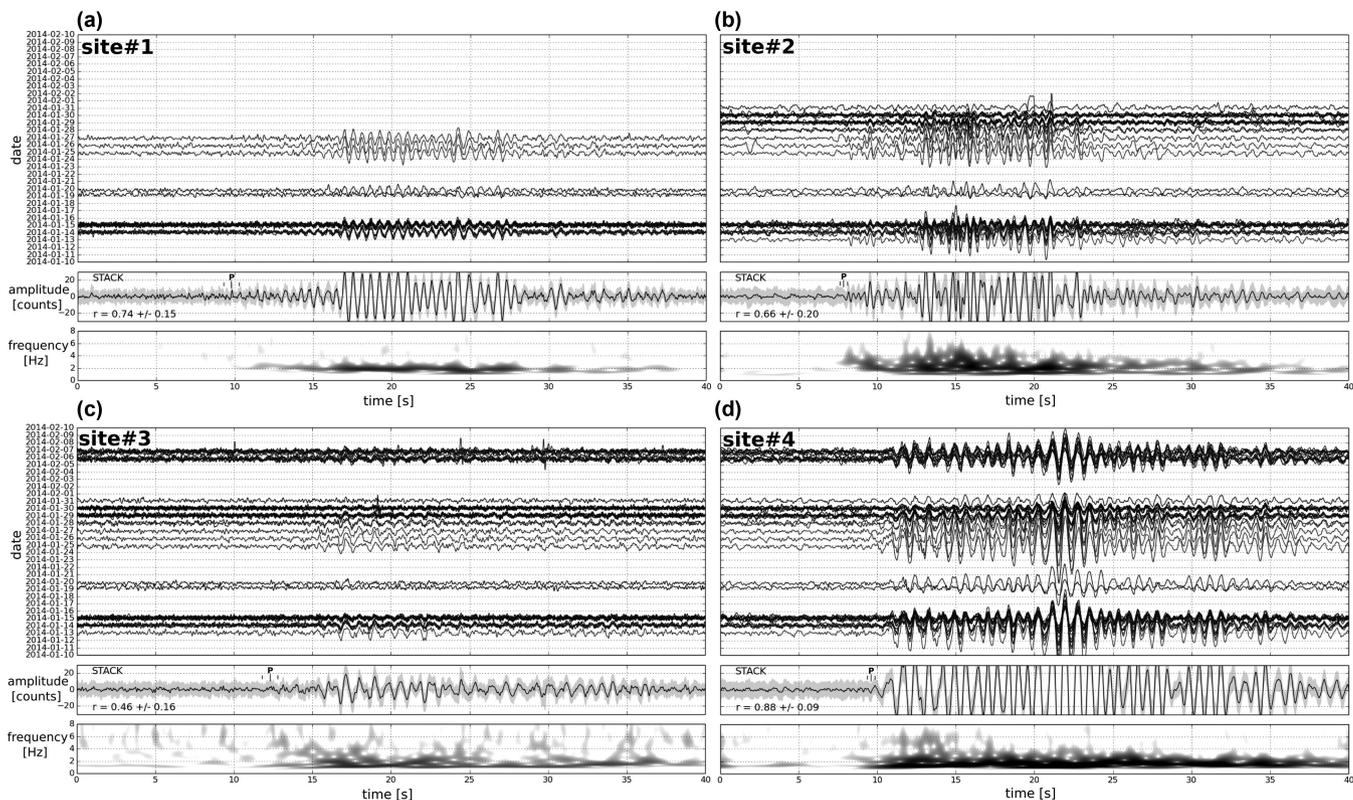
Figure 3. Seismic traces (vertical component) of the 48 LF events as a function of time. The seismic traces are bandpass filtered between 0.8 and 8 Hz. For each station site, the stack trace is shown below the 48 event data set. Each first *P*-wave arrival (denoted '*P*') and associated picking error (small vertical bars) are indicated on the stack trace. The mean correlation coefficient '*r*' between the 48 traces and the stack is given. The frequency spectrum is shown below each stack trace.

first *P*-wave arrival often followed by a lower frequency (<15 Hz) *S*-wave arrival with a maximum of 1 s delay (Fig. 2f). This observation implies that the event sources are located at a maximum of ∼4 km from the recording station (seismic velocities in the ice from Kohnen 1974). Indeed, those HF events are not identified at the next closest seismometer (∼10 km) and as a consequence cannot be located with precision. However, the continuous seismic record presents, for the two sites at grounding line zone (site#2 and site#3, Figs 2b and c), clear cycles of increased amplitude relative to the background noise level. In contrast, no or little increased amplitude is observed for the IRP site (site#1, Fig. 2a) and for the ice shelf site (site#4, Fig. 2d). Furthermore, for the latter we generally observe a larger time delay between the *P*- and the *S*-waves arrivals together with a relative lack of HF content implying larger source–station distance (Fig. 2f). This observation suggests that this seismic activity is predominant in the grounding line zone of the ice shelf shear margin (Fig. 1, black shaded zone). Such periods of heightened seismic activity are remarkably correlated in time and amplitude with downward motion of the ice shelf (Fig. 2e). An origin related to subglacial water outflow during falling tide may be discarded as this process would produce several minute or hour long seismic tremor signals rather than the observed few second long impulsive signals (Winberry *et al*. 2009a; Röösli *et al*. 2014; Bartholomaus *et al*. 2015). This seismic signature (short-duration, frequency content), the temporal and spatial occurrence of these seismic events strongly advocate an origin related to the flexure of the ice shelf during falling tides and accommodated by local surface crevassing. This would agree with the mechanism originally proposed by von der Osten-Woldenburg

(1990) and more recently by Barruol *et al*. (2013) based on long-duration seismic data sets recorded near an ice rumple (locally grounded ice, the flow of which matches the ice shelf flow) of the Ekström ice shelf and on a nunatak bordering the Mertz Glacier. An origin related to increased strain rate, as recently proposed by Podolskyi *et al*. (2016) for a grounded glacier of Greenland, may not be discarded as we observe eastward motion at site#4 during falling tide (not shown). However the amplitude of the latter remains relatively small (<0.15 m) compared to the amplitude of the flexure-induced vertical motion (>1.0 m). Akin to the observations of Barruol *et al*. (2013), initiation of seismicity appears to be related to the tide vertical velocity. At new spring tide when the tidal regime is diurnal or diurnal with a small semi-diurnal component, the velocity threshold varies between -0.05 and -0.15 m h^{-1}, in agreement with the velocity of ∼-0.1 m h^{-1} observed for the Metz Glacier diurnal tidal cycle (Barruol *et al*. 2013). This velocity threshold reaches -0.20 to -0.25 m h^{-1} at spring tide maximum for semi-diurnal tides (Supporting Information Fig. S1). These observations suggest that the tide-induced fracturing of the ice shelf is predominantly controlled by the tide velocity and the type of tidal regime (diurnal or semi-diurnal).

3.3 LF seismicity

In addition to this seismicity characterized by HF short-duration events, 48 other local events are detected through the 4 week period (Fig. 3). They are characterized by LF content (<5 Hz) and long duration (≥30 s). Each event produces seismic signal observable on the four sites with largest amplitudes recorded at site#2 and site#4
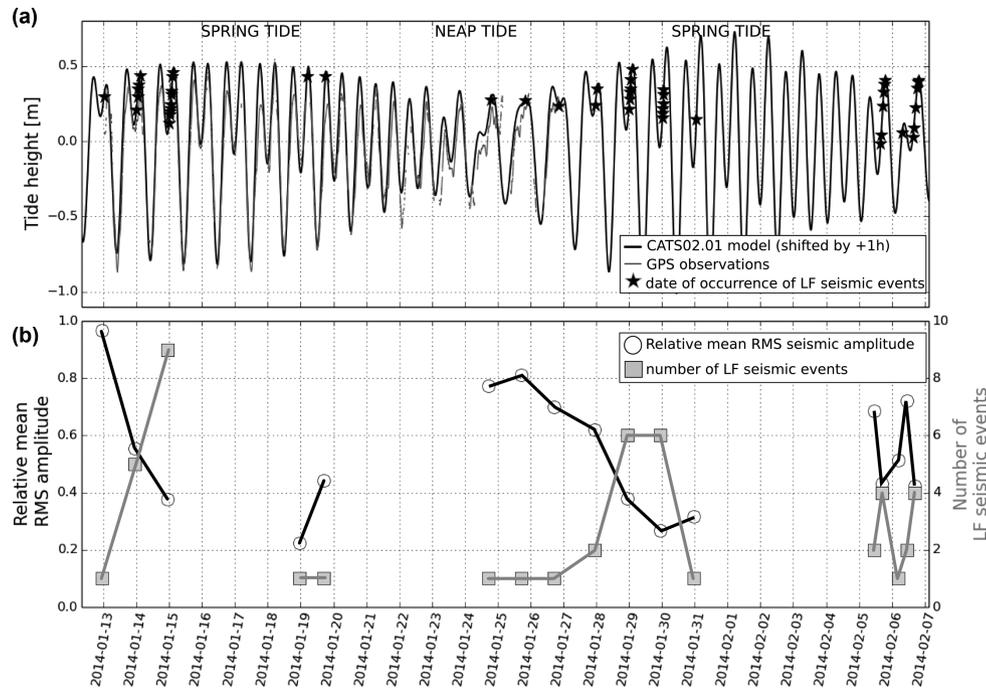
Figure 4. Temporal evolution of the 48 LF seismic events (black star) as a function of tide heights (a). Note for semi-diurnal tides, they occur only during the second, that is latest, rising leg of the tide. Temporal evolution of the mean RMS seismic amplitude (black open circle) and number of LF seismic events (grey square) as a function of time (b). They clearly present an anticorrelation pattern.

(Fig. 3). The amplitude of the first *P*-wave arrival was improved by stacking at each station individually the signals from the 48 events. The mean correlation coefficient between individual signal and the stack signal is greater than 0.6 for site#1, #2 and #4. The poorer value (0.44) found for site#3 results from lower signal-to-noise amplitude ratio. The remarkably similar seismic signature of these LF events suggests that they originate from the same source location and from the same source mechanism. The timing of the first seismic *P*-wave phase is characterized by maximum delay of 4 s between site#2 and site#3 leading to an apparent propagation velocity of ∼3.8 km s⁻¹, a value associated with *P*-wave propagation in the ice (Kohnen 1974). The timing of the *P*-wave phase resulting from stacking was picked on each stack trace and then used for the localization procedure. Considering the few available seismic stations, we use a simple non-iterative localization procedure (Inglada 1928). To provide an estimate of the localization error we varied 1-D *P*-wave velocity models (i.e. 3.6–4.0 km s⁻¹) and picking errors (0.25 s for site#2 and #4 and 0.5 s for site#1 and #3). The larger picking errors assigned to site#1 and #3 result from large uncertainties in picking their weak emergent signal. In turn, the picking errors contribute for about 2/3 to the final localization error. Numbers of obtained localizations falling in 1 × 1 km grid cell (or hit counts) were counted. Cells with largest hit count evidence the most probable event source location. A confidence region for the event source location was defined by the ensemble of grid cells having a total hit count falling within one standard deviation of the total hit count. This confidence region indicates the LF seismicity originates near the grounding line, similarly to the HF events, but here limited to the north of site#2 towards the ice shelf front (Fig. 1). Similarly to HF events, those 48 LF events exhibit a tidally paced behaviour. However, here, they rather show a fortnightly periodicity as they occur mostly, but not exclusively, during the first days of the neap-to-spring tide cycle, that is, when the tidal peak amplitude

increases again after the neap tide low amplitudes (Fig. 4). Only two small events are observed during spring-to-neap tide cycle (January 19th). Contrasting with the previously described HF events, these 48 LF events occur exclusively during rising tides and more particularly during the second, that is latest, rising leg of semi-diurnal tide (Fig. 4a). More specifically, this seismicity is characterized by a single large amplitude event at the beginning of the active period and by small clusters of smaller amplitude events (2–9 events 20–30 min apart) during the following days (Fig. 4). Interestingly, a clear anticorrelation pattern emerges between the number of events and their relative seismic amplitude (Fig. 4b). Though those observations are limited in time and firm conclusions on their origin would require longer data set they may deserve some discussion.

4 DISCUSSION

The occurrence of LF events only at rising tide suggests that an upward motion is required to trigger seismicity, though a displacement threshold does not clearly emerge from our observations (Fig. 4). The seismically active period is characterized by one initial major event at the beginning of the neap-to-spring tide cycle and by small clusters of smaller amplitude events in the next days. When the maximum of upward motion is reached at spring tide maximum no more seismic events are recorded and the spring-to-neap tide cycle is almost aseismic. Considering the above observations, the event location at the northern edge of the IRP, the low-frequency character of those events and the large area of detectability (at least 15 km from the source) we propose two hypotheses for their mechanism.

Regarding the first mechanism, the observed events may originate from basal crevassing of the ice shelf at the contact with the IRP. At the seaward side of the IRP, the high strain rate existing between the stable ice rise and the fast moving ice shelf combined with the

high tensile stresses resulting from the ice shelf fast velocity, thin ice shelf thickness may cause the formation of basal crevasses and eventually rifts (Matsuoka *et al.* 2015; Favier & Pattyn 2015) as it can be seen on Fig. 1 and as described by Nishio *et al.* (1984) and Pattyn *et al.* (2012). Progressive opening of basal crevasses by upward movement of the ice shelf during the first days of a new neap-to-spring tide cycle and their maximum opening at spring tide maximum could thus explain the temporal and amplitude pattern of our observations on LF seismic events. During the spring-to-neap tide cycle, as the tide height decreases, progressive crevasse closing would behave either as an aseismic process or generate insufficient seismic amplitude to be detected at distances considered here (i.e. >5 km). Similarly seismic events occurring at rising tide were recently observed on Antarctic ice shelves (Hammer *et al.* 2015) and were explained by a coupled mechanism of basal crevassing filled by ocean water exciting resonance resembling to observations from temperate glaciers of Alaska (West *et al.* 2010). However, such generated seismic events are of hybrid-type (HF signal followed by LF signal). Our LF events lacking HF content (>10 Hz) may express the lack of new crevasse opening resulting in resonance of water within the existing crevasses only (West *et al.* 2010) or our LF events are of hybrid-type but the HF content may be attenuated by a complex propagation and/or hidden within the background noise.

Regarding the second mechanism the observed events may originate from repeating slip on localized bedrock asperity close to the edge of the IRP. Such an interpretation relies primarily on observations of particular morphological features present at the northern edge of the IRP, coinciding with the location of the detected LF events, and on the hypothesis raised by Callens *et al.* (2014) on the presence of a sediment-covered bed found beneath the ice stream feeding the Roi Baudouin ice shelf. Indeed, while the presence of a steep topography for the ice sheet context (100 m elevation loss in less than 5 km) is a favourable condition for localized basal slip, the presence of a localized bedrock asperity whose surface expression, a blue ice field, is clearly visible on LIMA satellite images (Fig. 1) is a favourable condition for generating spatially concentrated seismicity. During the first days of each new neap-to-spring tide cycle, large amount of ocean water infiltrates into the bed of the IRP, lowering the friction between the bedrock and the overlying ice and initiates basal slip and the generation of an initial large amplitude seismic event. With further water infiltration due to successive high tide maxima, the bed weakens progressively due to water saturation of the sediment pores, the amplitude of the seismic events decreases but their number increases to accommodate for higher tide amplitude and higher water pressures of the spring tide maximum (Fig. 4b). After a couple of days, the bed is becoming sufficiently weakened and there is no more connection of the overlying ice with the bedrock preventing basal slip. No seismic events occur. During the spring-to-neap tide cycle, the bed strengthened again as most of the ocean water outflows from the IRP bed. This scenario would be consistent with the observation of lower seismic energy released by deforming bed as observed by Smith (2006) on the Rutford Ice Stream. Furthermore, this hypothesis would bear resemblances with other observations of seismicity controlled either by variations in subglacial drainage in the ablation zone of Greenland (Röösli *et al.* 2016) or by ice stream basal stress modulation from ocean tides (Anandakrishnan & Alley 1997; Wiens *et al.* 2008; Winberry *et al.* 2009b, Zoet *et al.* 2012). However it differs from other stick-slip observations in Antarctica where seismicity is detected for both spring and neap tides (e.g. Winberry *et al.* 2009b). Antarctic basal events have been identified through the detection of a broad

variety of seismic signals (Blankenship *et al.* 1987; Anandakrishnan & Alley 1997; Smith 2006, Danesi *et al.* 2007; Wiens *et al.* 2008; Zoet *et al.* 2012; Winberry *et al.* 2013). Therefore, the existence of basal slip should be invoked using another independent data set such as surface displacement measurements. However, the GPS device of site#2, the closest (max ∼15 km) to the identified source region of such seismicity, does not present any horizontal ice flow acceleration (Fig. 2b). So if basal slip exists here it may be confined to an area limited to a couple of km around the bedrock asperity. Other explanations may be proposed: either basal slip is too small to be recorded at surface (the resolution is 3.5 cm on the calculated horizontal position) and/or it is entirely accommodated by internal deformation of basal sediments or of the ice layer or/and by the presence of the highly fractured margin zone.

Though both interpretations remain speculative, we believe that such LF seismic events warrant further investigations as they may offer important new information on the ice-shelf–ocean interactions. Combining finer network geometry and longer data set spanning several neap-to-spring tide cycles would provide further support on the location and the fortnightly modulation of such seismicity.

5 CONCLUSIONS

Using a low-cost, light-weight, low-consumption instrument capable of recording simultaneously displacement (embedded GPS receiver) and seismic velocity (external seismometer) our study shows the impact of the tidal forcing on an Antarctic ice shelf lateral margin. A diurnal tide-modulated HF seismicity is found to be confined to the grounding line zone and is associated with the flexure of the ice shelf at its lateral margin. An apparent fortnightly modulated LF seismicity is localized at the contact of the IRP with the ice shelf front where basal mechanisms (crevassing or slip on a bedrock asperity) may be controlled by a surge of ocean water at bed at new spring tide. These findings provide new insights into the identification of most vulnerable zones of the ice shelf margin. We advocate a multiplicity of comparable geophysical experiments on a long-term basis in order to improve our knowledge of ice shelves and better assess their vulnerability to ocean forcing.

REFERENCES

Allen, R.V., 1978. Automatic earthquake recognition and timing from single traces, *Bull. seism. Soc. Am.,* **68,** 1521–1532

Anandakrishnan, S. & Alley, R.B., 1997. Tidal forcing of basal seismicity of ice stream C, West Antarctica, observed far inland, *J. geophys. Res.,* **102,** 1–15.

Barruol, G., Cordier, E., Bascou, J., Fontaine, F.R., Legresy, B. & Lescarmontier, L., 2013. Tide-induced microseismicity in the Mertz glacier grounding area, East Antarctica, *Geophys. Res. Lett.,* **40,** 5412–5416.

Bartholomaus, T.C., Amundson, J.M., Walter, J.I., O'Neel, S., West, M.E. & Larsen, C.F., 2015. Subglacial discharge at tidewater glaciers revealed by seismic tremor, *Geophys. Res. Lett.,* **42,** 6391–6398.

Benoit, L. *et al.,* 2015a. Multi-method monitoring of Glacier d'Argentière dynamics, *Ann. Glaciol.,* **56,** 118–128.

Benoit, L., Briole, P., Martin, O., Thom, C., Malet, J.P. & Ulrich, P., 2015b. Monitoring landslide displacements with the Geocube wireless network of low-cost GPS, *Eng. Geol.,* **195,** 111–121.

Beyreuther, M., Barsch, R., Krischer, L., Megies, T., Behr, Y. & Wassermann, J., 2010. ObsPy: a python toolbox for seismology, *Seismol. Res. Lett.,* **81**(3), 530–533.

Bindschadler, R. *et al.,* 2008. The landsat image mosaic of Antarctica, *Remote Sens. Environ.,* **112,** 4214–4226.

Blankenship, D.D., Anandakrishnan, S., Kempf, J.L. & Bentley, C.R., 1987. Microearthquakes under and alongside ice stream B, Antarctica, detected by a new passive seismic array, *Ann. Glaciol.,* **9,** 30–34.

Callens, D., Matsuoka, K., Steinhage, D., Smith, B., Witrant, E. & Pattyn, F., 2014. Transition of flow regime along a marine-terminating outlet glacier in East Antarctica, *Cryosphere,* **8,** 867–875.

Callens, D., Thonnard, N., Lenaerts, J., van de Berg, W.J., Matsuoka, K. & Pattyn, F., 2015. Mass balance of the Sør Rondane Glacier System, East Antarctica, *Ann. Glaciol.,* **56**(70), 63–69.

Danesi, S., Bannister, S. & Morelli, A., 2007. Repeating earthquakes from rupture of an asperity under an Antarctic outlet glacier, *Earth planet. Sci. Lett.,* **253,** 151–158.

Drews, R., Martín, C., Steinhage, D. & Eisen, O., 2013. Characterizing the glaciological conditions at Halvfarryggen ice dome, Dronning Maud Land, Antarctica, *J. Glaciol.,* **59**(213), 9–20.

Drews, R., Matsuoka, K., Martín, C., Callens, D., Bergeot, N. & Pattyn, F., 2015. Evolution of Derwael Ice Rise in Dronning Maud Land, Antarctica, over the last millennia, *J. geophys. Res.,* **120,** 1–16.

Favier, L. & Pattyn, F., 2015. Antarctic ice rise formation, evolution, and stability, *Geophys. Res. Lett.,* **42,** 4456–4463.

Hammer, C., Ohrnberger, M. & Schlindwein, V., 2015. Pattern of cryospheric seismic events observed at Ekström Ice Shelf, Antarctica, *Geophys. Res. Lett.,* **42,** 3936–3943.

Hunter, J.D., 2007. Matplotlib: a 2D graphics environment, *Comput. Sci. Eng.,* **9,** 90–95.

Inglada, V., 1928. Die berechnung der herdkoordinated eines nahbebens aus den eintrittszeiten der in einingen benachbarten stationen aufgezeichneten P-oder P-wellen, *Gerlands Beitr. Geophys.,* **19,** 73–98.

Kim, K.T., Jezek, K.C. & Sohn, H.G., 2001. Ice shelf advance and retreat rates along the coast of Queen Maud Land, Antarctica, *J. geophys. Res.,* **106**(C4), 7097–7106.

Kohnen, H., 1974. The temperature dependence of seismic waves in ice, *J. Glaciol.,* **13,** 144–147.

Matsuoka, K., Pattyn, F., Callens, D. & Conway, H., 2012. Radar characterization of the basal interface across the grounding zone of an ice-rise promontory in East Antarctica, *Ann. Glaciol.,* **53**(60), 29–34.

Matsuoka, K. *et al.,* 2015. Antarctic ice rises and rumples: their properties and significance for ice-sheet dynamics and evolution, *Earth-Sci. Rev.,* **150,** 724–745.

Nishio, F., Ishikawa, M., Ohmae, H., Takahashi, S. & Katsushima, T., 1984. A preliminary study of glacial geomorphology in area between Breid Bay and the Sør Rondane Mountains in Queen Maud Land, East Antarctica, *Nankyoku Shiryô,* **83,** 11–28.

Padman, L., Fricker, H., Coleman, R., Howard, S. & Erofeeva, L., 2002. A new tide model for the Antarctic ice shelves and seas, *Ann. Glaciol.,* **34,** 247–254.

Pattyn, F. *et al.,* 2012. Melting and refreezing beneath Roi Baudouin Ice Shelf (East Antarctica) inferred from radar, GPS, and ice core data, *J. geophys. Res.,* **117,** F04008, doi:10.1029/2011JF002154.

Podolskyi, E.A., Sugiyama, S., Funk, M., Walter, F., Genco, R., Tsutaki, S., Minowa, M. & Ripepe, M., 2016. Tide-modulated ice flow variations drive seismicity near the calving front of Bowdoin Glacier, Greenland, *Geophys. Res. Lett.,* **43,** 2036–2044.

Remondi, B.W. & Brown, G., 2000. Triple differencing with Kalman filtering: making it work, *GPS Solut.,* **3**(3), 58–64.

Rignot, E., Mouginot, J. & Scheuchl, B., 2011. Ice flow of the antarctic ice sheet, *Science,* **333**(6048), 1427–1430.

Röösli, C., Walter, F., Husen, S., Andrews, L.C., Lüthi, M.P., Catania, G.A. & Kissling, E., 2014. Sustained seismic tremors and icequakes detected in the ablation zone of the Greenland ice sheet, *J. Glaciol.,* **60**(221), 563–575.

Röösli, C., Helmstetter, A., Walter, F. & Kissling, E., 2016. Meltwater influences on deep stick-slip icequakes near the base of the Greenland Ice Sheet, *J. geophys. Res. Earth Surf.,* **121**(2), 223–240.

Smith, A.M., 2006. Microearthquakes and subglacial conditions, *Geophys. Res. Lett.,* **33**(24), L24501, doi:10.1029/2006GL028207.

von der Osten-Woldenburg, H., 1990. Icequakes on Ekström Ice Shelf near Atka Bay, Antarctica, *J. Glaciol.,* **36**(122), 31–36.

West, M.E., Larsen, C.F., Truffer, M., O'Neel, S. & LeBlanc, L., 2010. Glacier microseismicity, *Geology,* **38**(4), 319–322.

Wiens, D.A., Anandakrishnan, S., Winberry, J.P. & King, M.A., 2008. Simultaneous teleseismic and geodetic observations of the stick–slip motion of an Antarctic ice stream, *Nature,* **453,** 770–774.

Winberry, J.P., Anandakrishnan, S. & Alley, R.B., 2009a. Seismic observations of transient subglacial water-flow beneath MacAyeal Ice Stream, West Antarctica, *Geophys. Res. Lett.,* **36,** L11502, doi:10.1029/2009GL037730.

Winberry, J.P., Anandakrishnan, S., Alley, R.B., Bindschadler, R.A. & King, M.A., 2009b. Basal mechanisms of ice streams: insights from the stick-slip motion of Whillans Ice Stream, West Antarctica, *J. geophys. Res.,* **114,** F01016, doi:10.1029/2008JF001035.

Winberry, J.P., Anandakrishnan, S., Wiens, D.A. & Alley, R.B., 2013. Nucleation and seismic tremor associated with the glacial earthquakes of Whillans Ice Stream, Antarctica, *Geophys. Res. Lett.,* **40,** 312–315.

Zoet, L.K., Anandakrishnan, S., Alley, R.B., Nyblade, A.A. & Wiens, D.A., 2012. Motion of an Antarctic glacier by repeated tidally modulated earthquakes, *Nat. Geosci.,* **5**(9), 623–626.

SUPPORTING INFORMATION

Additional Supporting Information may be found in the online version of this paper:

Figure S1. Temporal evolution of the HF seismicity and falling tide characteristics. The tide velocity is the time derivative of the CATS02.01 tide height model, which is +1 hr shifted to match the tide phase observed at site#4 (a). The tide velocity is negative as motion is downward for falling tides. The falling tide downward displacement prior to the initiation of seismicity remains relatively small (<30 cm) and presents no clear trend (b). Duration (c) and amplitude (d) of seismicity show largest values for largest falling tide duration during the neap-to-spring tide cycle. (http://gji.oxfordjournals.org/lookup/suppl/doi:10.1093/gji/ggw214/-/DC1).

Please note: Oxford University Press is not responsible for the content or functionality of any supporting materials supplied by the authors. Any queries (other than missing material) should be directed to the corresponding author for the paper.